THE ASTROPHYSICAL JOURNAL, 475:665–682, 1997 February 1
© 1997. The American Astronomical Society. All rights reserved. Printed in U.S.A.

X-RAY EMISSION-LINE IMAGING AND SPECTROSCOPY OF TYCHO's SUPERNOVA REMNANT

U. HWANG AND E. V. GOTTHELF[1]
NASA/Goddard Space Flight Center, Greenbelt, MD 20771; hwang@rosserv.gsfc.nasa.gov, gotthelf@gsfc.nasa.gov
Received 1995 November 14; accepted 1996 August 26

ABSTRACT

We present X-ray images of Tycho's supernova remnant in emission-line features of Mg, Si, S, Ar, Ca, and Fe, plus the continuum, using data obtained by the imaging spectrometers on board the *Advanced Satellite for Cosmology and Astrophysics* (*ASCA*). All the images show the shell-like morphology characteristic of previously obtained broadband X-ray images, but they are clearly distinct from each other. We use image reconstruction techniques to achieve a spatial resolution of $\sim 0.'8$. Line intensity ratios are used to make inferences about the remnant's physical state, on average for the entire remnant and with angular position around the rim. The average temperature of the Si and S ejecta in the remnant is (0.8–1.1) $\times 10^7$ K, and the average ionization age is (0.8–1.3) $\times 10^{11}$ cm^{-3} s. For a constant ionization age, the observed relative brightness variations of Si and S line image profiles with azimuthal angle imply differences of roughly a factor of 1.3–1.8 in the temperature. We compare the radial brightness profiles of our images with simple geometrical models and find that a spherical emitting geometry is favored over a torus. A spherical geometry is further supported by the absence of systematic Doppler shifts across the remnant. The radial fit results also suggest that some radial mixing of the ejecta has occurred. However, the azimuthally averaged Fe K image peaks at a markedly lower radius than the other images. The average Fe K/Fe L line intensity ratio and the position of the Fe K energy centroid support a temperature several times higher and an ionization age approximately a factor of 10 lower than for the other elements, and imply that the Fe ejecta must have retained some of its stratification. Although many of the features in the 4–6 keV X-ray continuum correspond to those in the radio, there is no obvious correlation between the relative brightness in these bands.

Subject headings: ISM: individual (Tycho's Supernova) — supernova remnants — X-rays: ISM

1. INTRODUCTION

The remnant of the supernova recorded in 1572 by Tycho Brahe is the standard of Type Ia remnants and one of the most extensively studied at all wavelengths. Hamilton, Sarazin, & Szymkowiak (1986) present a detailed X-ray spectral study and provide an excellent summary of the observations as of 1986. More recent work is presented on X-ray spectra by Tsunemi et al. (1986), Smith et al. (1988), and Fink et al. (1994), on X-ray imaging by Vancura, Gorenstein, & Hughes (1995), in the optical by Kirshner, Winkler, & Chevalier (1987), Teske (1990), and Smith et al. (1991), and in the radio by Dickel, van Breugel, & Strom (1991) and Wood, Mufson, & Dickel (1992). Hydrodynamical simulations for the X-ray spectra were carried out by Itoh, Masai, & Nomoto (1988) and Brinkmann et al. (1989).

At an age of just over 400 yr, Tycho is a relatively young remnant and is still dominated in X-rays by emission from its ejecta. The evidence for this is twofold: line strengths require abundances in excess of the solar value regardless of the ionization state or temperature of the gas (Hamilton et al. 1986), while the mass of ejecta and shocked interstellar medium (ISM) are estimated to be roughly equal (Seward, Gorenstein, & Tucker 1983). Tycho is therefore an excellent target to investigate the spatial distribution of the ejecta.

Until recently, however, no single X-ray instrument has combined the spectral and spatial resolution required for such a study. Observations with previous imaging spectrometers and pointed observations with instruments having small fields of view did not reveal any significant changes in the spectrum across the Tycho remnant (Reid, Becker, & Long 1982; Szymkowiak 1985). Vancura et al. (1995) exploited the different bandpasses of the *Einstein* and *ROSAT* high-resolution imagers (HRIs) to search for spatial differences in two energy bands: one dominated by Si and Fe, the other by Si and S. They concluded that the differences they observe are likely due to differences in the distribution of elements in the ejecta. The two solid-state imaging spectrometers (SISs) on the *Advanced Satellite for Cosmology and Astrophysics* (*ASCA*) (Tanaka, Inoue, & Holt 1994) are the first X-ray instruments to directly image extended sources in relatively narrow energy bands dominated by emission lines of individual elements. In this paper, we present narrowband images of Tycho from the SISs for all the prominent features in the SIS spectrum (§ 2). Tycho has a diameter of 8′ that fits well within the SIS field of view and is adequately large compared with the spatial resolution of the mirrors for study of the X-ray spatial structure.

Spatial structure in emission-line images could result from variations in density, temperature, ionization age, or column density, as well as in the element abundances. We therefore use a model where the X-ray–emitting plasma is characterized by these parameters. The ionization age of the gas is defined as nt, where n is the electron density and t is the time since the gas was heated by the passage of the shock front. At the low electron densities characteristic of X-ray bright supernova remnants, the timescale for achieving the equilibrium ionization state is generally larger than the known or estimated age of the remnant itself, and most remnants are unlikely to be in ionization equilibrium (Gorenstein, Harnden, & Tucker 1974). This nonequilib-

[1] Universities Space Research Association.

rium ionization state can have important effects on the spectrum, particularly in enhancing the line emission from stable, abundant ions, and therefore its effects must be considered for supernova remnants (Gronenschild & Mewe 1982).

The values of the temperature and ionization age are constrained for a given column density by the ratios of measured line intensities. For low-density plasmas, the line ratios are not strongly density-dependent. We use the global X-ray spectrum to constrain the spatially averaged value of physical quantities as a benchmark against which to measure spatial variations, and also to correct for the fraction of the counts in each image that are not due to the emission line of interest but rather to the underlying continuum or to nearby emission lines (§ 3). We then use the ratios of azimuthal intensity profiles of the images to study the variation of these parameters with position in the remnant (§ 4.1). We choose to study the azimuthal distributions given Tycho's shell-like morphology.

The radial structure in the images is investigated by fitting simple models for the three-dimensional structure of the emission (§ 4.2). We also carry out a search for a spatial pattern in the line energies that is due to Doppler velocity shifts (§ 5).

Preliminary results of this work are presented by Gotthelf & Hwang (1996). We find modest variations in the spectral parameters for the ejecta with position in the remnant, and support for a spherical emitting geometry. The azimuthally averaged Fe K emission is found to peak at a lower radius than the emission in other features, including the continuum. The relative Fe line intensities and the Fe K centroid support physically different conditions for Fe than the other elements, and imply that the Fe ejecta must have retained some of its stratification.

2. SPECTRAL IMAGES

2.1. *Observations and Procedures*

ASCA (Tanaka et al. 1994) has four imaging spectrometers, each in the focal plane of its own telescope: two solid-state imaging spectrometers (SIS0 and SIS1) with slightly offset $22' \times 22'$ fields of view, each composed of square arrays of four CCD chips, and two gas imaging spectrometers (GIS). The SIS has a spectral resolution of 2% at 6 keV that scales like $\sim E^{-1/2}$ over the energy range 0.4–10 keV.[2] The spatial resolution of the SIS is limited by the X-ray mirrors, whose azimuthally averaged point-spread function (PSF) is characterized by a narrow core of FWHM 50″ on the optical axis with extended wings giving a half-power diameter of 3′ (Jalota, Gotthelf, & Zoonematkermani 1993). The GIS has a higher effective area above 5 keV than the SIS, but it has worse spectral and spatial resolution. We focus on the SIS herein but use the GIS to support the SIS results.

The Tycho supernova remnant (SNR) was observed by the instruments on board *ASCA* on 1993 August 29 during the performance verification phase of the mission. We obtained these data from the public archive. For these observations, the four CCDs of each SIS sensor were exposed in pairs (2-CCD mode) or simultaneously (4-CCD mode), and the data were collected almost exclusively in BRIGHT mode (we refer the reader to the ABC Guide for *ASCA* analysis, Day et al. 1995, for definitions of *ASCA* terms and detailed guidelines for data selection and reduction). The data were selected to exclude times of high background contamination using standard selection criteria for an effective observation time of 44 ks for the two sensors combined. None of the time-filtered SIS data included telemetry-saturated CCD readout frames. Hot and flickering pixels were identified and removed using the CLEANSIS algorithm (Gotthelf 1993).

Images were generated by aligning and adding exposure-corrected images in both 2-CCD mode and 4-CCD mode from the two SIS instruments. There are some differences in spectral resolution and gain between data taken in 2-CCD mode and data taken in 4-CCD mode, but these are not critical for the images. These effects involve primarily the details of the spectral response to a narrow emission line, and while they therefore affect the results of a spectral fit, they will not significantly affect an image where the photon energies have a range of a few hundred eV or more. Exposure maps were generated with ASCAEXPO (Gotthelf 1994), which uses the aspect solutions, chip alignment, and hot pixel maps to determine the exposure time for each sky image pixel. The resultant smoothed broadband image, scaled to retain the original number of total image counts, is displayed in Figure 1*a*.

2.2. *Image Restoration*

The broadband image was further processed with the Lucy-Richardson image restoration algorithm (Lucy 1974; Richardson 1972) to remove the effects of the broad wings in the PSF and to improve the effective spatial resolution and contrast. We used the ray-traced, on-axis point response function (Jalota et al. 1993) as the kernel for our deconvolution. This PSF is reasonable for the combined image of Tycho from the two SIS instruments. The optical axes of the two instruments are offset by $\sim 5'$, and the mean optical axis is centered on the remnant image; variations of the PSF across the 8′ diameter remnant therefore tend to average out. Moreover, we find that the deconvolution is relatively insensitive to the fine details of the PSF used, since the PSF changes slowly with position over the image of Tycho and with energy. We iterate the Lucy-Richardson algorithm to produce an effective spatial resolution comparable to the $\sim 50''$ FWHM core of the PSF. Even with a conservative number of iterations, the algorithm allows us to increase the image contrast by approximately a factor of 4 without introducing artifacts. This was demonstrated in the *ASCA* analysis of close point sources (Gotthelf et al. 1994) and of extended emission in the Cas A supernova remnant (Holt et al. 1994), and is further discussed below. The application of this technique to the broadband SIS image of Tycho's SNR is displayed in Figure 1*b*.

In the remainder of this section, we test the photometric robustness of our restored images. As a first example, the restored SIS image is compared with the *ROSAT* Position Sensitive Proportional Counter (PSPC) image. We show the PSPC image at energies above 1 keV in Figure 2*a*, smoothed to the spatial resolution of the deconvolved SIS images. The SIS image shown in Figure 2*b* weights the image according to the ratio of the PSPC and the SIS effective areas as a function of pulse height for energies above 1 keV, and is in effect a simulation of the PSPC image with the SIS data. The two images are reassuringly similar, with the main features reproduced by both instruments. There

[2] Resolution at launch.

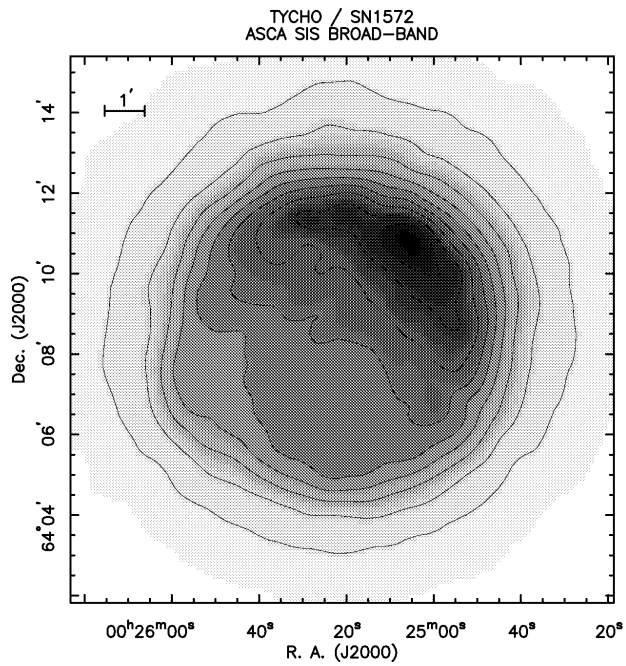

FIG. 1*a*

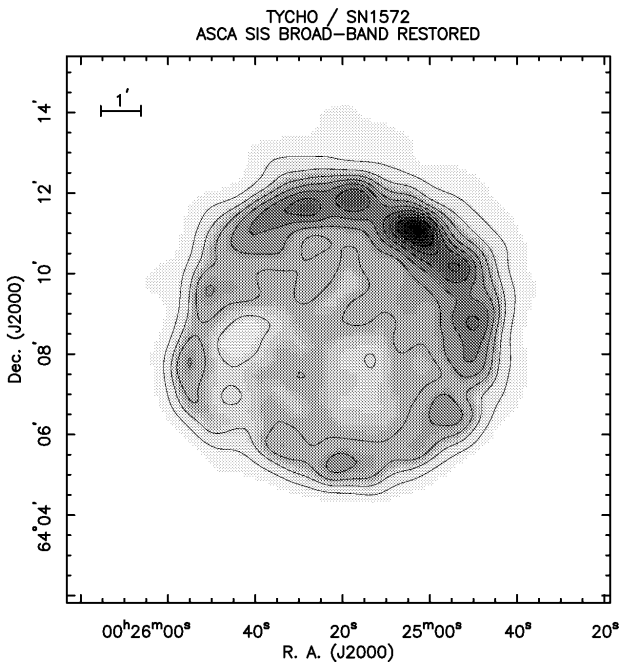

FIG. 1*b*

FIG. 1.—(*a*) The smoothed, exposure-corrected broadband *ASCA* SIS image of Tycho with contours overlaid. The increment in intensity between contours is 10% of the total intensity. The image is centered on the coordinates J2000 R.A. = $00^h25^m21^s$, decl. = 64°08′.6. (*b*) The same image after restoration with 100 iterations of the Lucy-Richardson deconvolution algorithm.

are slight differences between the images, which are to be expected considering the difference in the spatial and spectral resolution of the two instruments and the restoration applied to the SIS image. As an example, the normalized cumulative azimuthal profiles for radii between 2′ and 5′ in 10° angular bins show deviations of no more than 1%.

Next we considered the effect of the number of image counts on the morphology, especially of bright features. Restored narrowband images in the Si Heα line were generated with progressively fewer counts by randomly excluding a fraction of counts from the original event files. We find that undeconvolved images with fewer than ~ 5 counts pixel^{-1} (where pixels are correlated on the $\sim 1'$ length scale of the PSF core) are mottled on arcminute scales and that individual bright spots do not necessarily represent true localized features. This is consistent with expectations from Poissonian statistics. We stress that bright spots are not artifacts of the deconvolution (compare Figs. 4*a* and 4*b* discussed in § 2.3). These bright spots are also evident in the original images, but in those cases with few total counts per spatial resolution element, they may reflect statistical fluctuations rather than real features. The deconvolution merely sharpens the images, and bright features in the deconvolved image have a one-to-one correspondence to features in the original images. We avoid the noise amplification caused by overiterating the Lucy algorithm by just iterating the algorithm to restore the images to the $\sim 1'$ scale of the PSF core.

In the narrowband images of Tycho presented in the next section, images with greater than $\sim 20{,}000$ counts (as given in Table 1, § 2.3) are considered photometric representations of the X-ray morphology on 1′ length scales. Images with fewer total counts are accurate only on progressively larger scale sizes, since their bright arcminute features may

TABLE 1

ENERGY CUTS FOR IMAGES

Image	Spectral Feature	PI Energy Range (keV)	Counts ($\times 10^3$)	Deconvolution Iterations
1	Low energy	0.40–0.77	45	40
2	Fe L blend I	0.77–1.02	117	40
3	Fe L blend II	1.02–1.28	108	40
4	Mg Heα, Fe L	1.28–1.39	41	40
5	Low-energy continuum	1.39–1.72	78	40
6	Si He α	1.72–1.97	247	100
7	Si He $3p + 4p$	1.97–2.30	72	40
8	S He α	2.30–2.56	64	40
9	S He $3p + 4p$, Ar Heα	2.74–3.25	25	20
10.....	Ca Heα	3.71–4.22	21[a]	20
11.....	High-energy continuum	4.22–6.19	23[a]	20
12.....	Fe Kα	6.19–6.85	5.3[a]	10

[a] Relaxed time-filtering criteria.

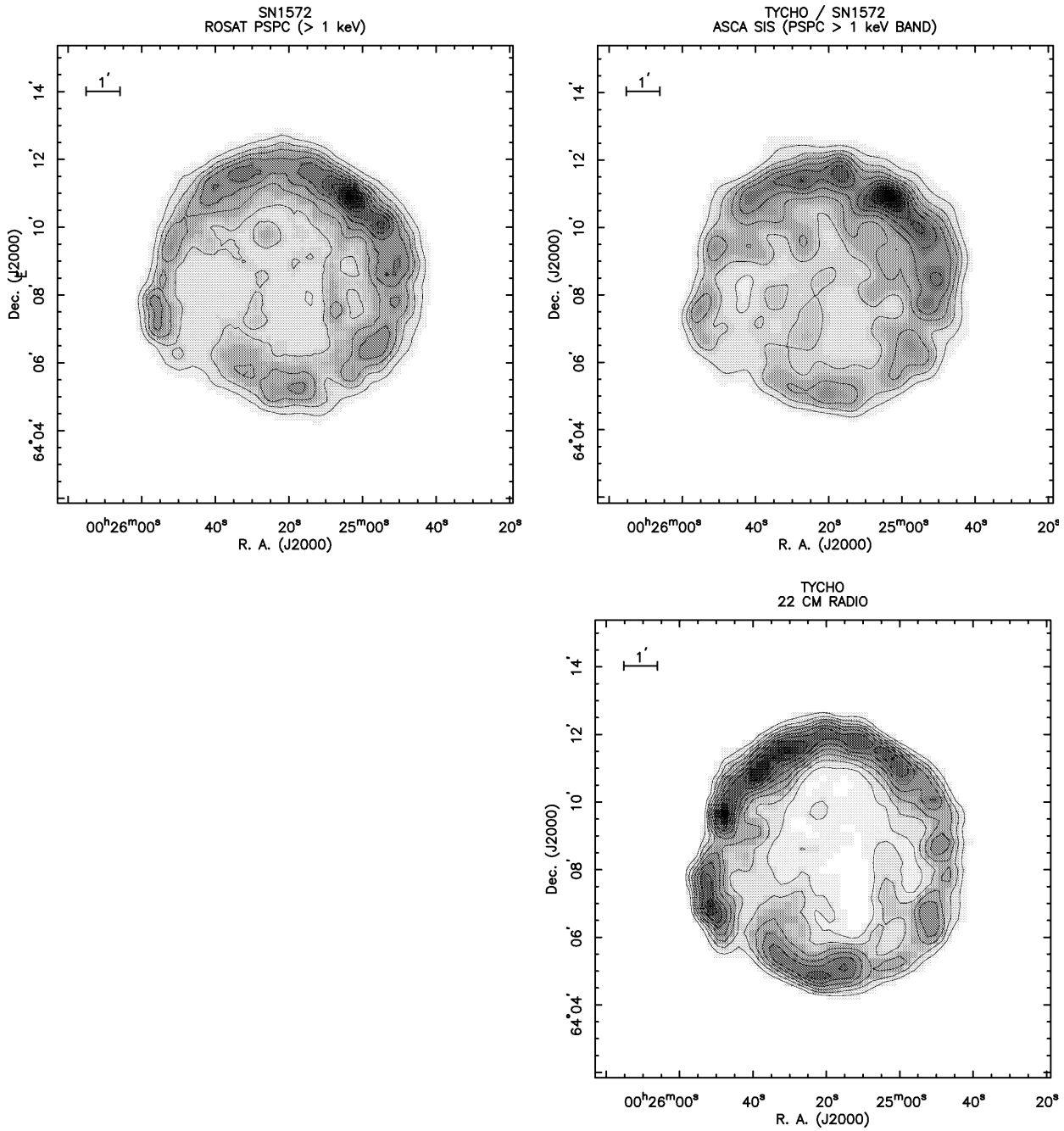

FIG. 2.—*Top left*: *ROSAT* PSPC X-ray image of Tycho at energies above 1 keV smoothed to the *ASCA* spatial resolution. *Top right*: *ASCA* SIS image in the *ROSAT* PSPC passband, compensating for the relative effective areas of the PSPC and SIS. *Bottom:* 22 cm VLA radio image (courtesy of J. Dickel) smoothed to the *ASCA* spatial resolution. The contours show linear 10% intensity increments.

be due to statistical fluctuations. Scaling the length scale to the total number of counts, an image with ~ 5000 counts has believable features on $\gtrsim 2'$ scales.

2.3. *Narrowband Images*

Narrowband images were formed by using the spatially integrated SIS spectrum to select appropriate pulse-height cuts. Pulse-height spectra were extracted from the same circular region of radius 5′ for both SIS0 and SIS1. This region spans all four chips of each SIS sensor, so the gains of individual chips were adjusted using the calibration file of 1994 July 28 to allow the combination of spectra from individual chips. A composite spectrum of Tycho in which all the SIS data (4-CCD mode) have been combined for display is shown in Figure 3. Smoothed and exposure-corrected images for each distinguishable spectral feature are shown in Figure 4*a* (see Fig. 4*d* [Pl. 29]). The energy ranges and labels for each image are given in Table 1. The last three images listed in Table 1 were formed with relaxed time-filtering selection criteria in order to maximize the number of counts. This procedure is justified since the relative instrumental background is significantly lower at these higher energies.

The spectrum is dominated by the Si Heα blend ($n = 2$ to $n = 1$ in the He-like ion; see Table 2 for line definitions and energies). The Heα features of S, Ar, and Ca are also prominent, as are the Kα ($n = 2$ to $n = 1$ in all ions) blend of Fe, and other blends of Si and S (He $1s3p \rightarrow 1s^2$ and He

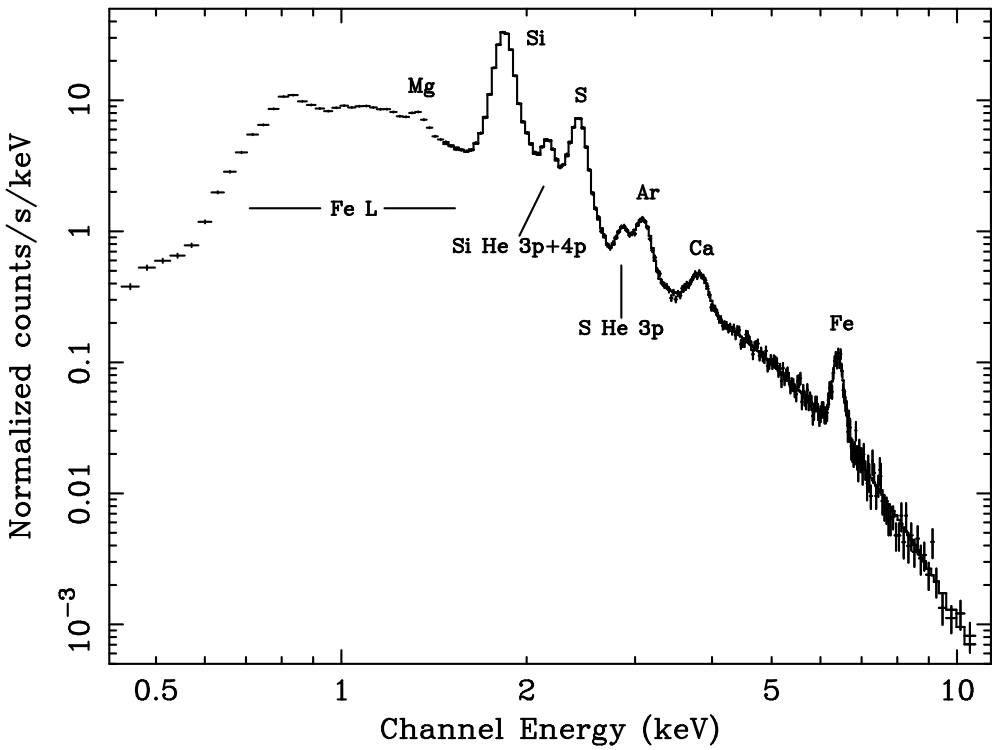

FIG. 3.—X-ray spectrum of Tycho obtained with the *ASCA* SISs in 4-CCD mode, wherein data from both sensors (SIS0 and SIS1) have been combined for display. The prominent emission blends are labeled (see Table 2 for line transitions), with the Heα ($n = 2$ to $n = 1$) blends indicated by element. The best-fit model for continuum plus Gaussian lines for $E > 1.5$ keV is shown overlaid as a visual aid.

$1s4p \rightarrow 1s^2$). The strong Heα blends of Si and S dwarf the nearby Lyα lines, which are not resolved. There is also a hint of the Mg Heα blend, but this feature may be partially due to Fe. Most of the emission below about 1.4 keV is line emission that the SIS is unable to resolve, and is attributable primarily to numerous Fe L transitions. Only the narrow energy regions between 1.4 and 1.7 keV, between 4 and 6 keV, and above 8 keV are nearly free of line emission.

The restored narrowband images (Fig. 4*b* [see Fig. 4*e* (Pl. 30)]; see Table 1 for energy cuts) all show the shell structure characteristic of the broadband X-ray image, with the possible exception of the image in Fe K. The shell can be traced around most of the periphery of the remnant, while the positions of the brightness enhancements vary from image to image. The angular scale at which bright clumps are resolved is limited by the image restoration. Differences in the relative brightness are clearly distinguished in several images. Notably, the Si and S images are bright to the north and west, while the Ca image is bright only in the west and the 4–6 keV continuum is bright in the southwest. The flat-fielded images in the GIS that correspond approximately to the pulse-height cuts used for the SIS narrowband images have brightness distributions that match those of the SIS images to the lower spatial resolution (2′–3′) of the GIS (see Fig. 4*c* [see Fig. 4*f* (Pl. 31)]). In particular, the increased signal in the GIS at high energies supports the SIS results for Ca, the 4–6 keV continuum, and Fe K.

The Fe K image does not show the smooth shell structure characteristic of the other images, although its average radial extent is roughly the same. The clumpiness is due partially to the much fewer number of counts in this image relative to the others (see Table 1 and discussion in § 2.2). The image suggests a lumpy ring with its northern and eastern boundaries interior to the periphery of the shell in other images, and a knot breaking out to the southeast (see the overlay with Fe L in Fig. 5*a*).

The X-ray emission in the 4–6 keV range is primarily continuum emission. The X-ray image shows a faint ring with an extensive bright enhancement on the western rim. Existing radio maps (e.g., 6 and 22 cm, Dickel et al. 1991; 11 cm, Dickel & Jones 1985; 21 cm, Strom, Goss, & Shaver 1982) show the radio surface brightness peaking strongly to the east, northeast, and south. Figure 2*c* shows a 22 cm VLA radio image of Tycho (kindly provided by J. Dickel) smoothed to the *ASCA* spatial resolution. The images do show general correspondence in the position of X-ray and radio features, but they show no correlation in their relative brightness. Along the eastern half of the remnant where the radio emission is bright, the X-ray features are faint, while there is only a hint of a radio feature at the position of the bright X-ray enhancement to the west. The lack of correlation between the brightness in the radio and the X-ray continuum contrasts with the Type II remnant Cas A (Holt et al. 1994), where the X-ray continuum brightness follows the radio brightness. There is evidently a different relationship between the X-ray and the radio continua in these two remnants. The excellent correspondence between the radio and the X-ray peripheries of Tycho (Dickel et al. 1991; Seward et al. 1983) indicates, nevertheless, that both the radio and the X-ray emission occur via processes in the shock wave.

A bright, isolated knot appears in several of our images near the southeast bulge. The features in Fe L, Mg/Fe, and Fe K are farther south than a similar feature in the Si and S images (see Fig. 5*b* and azimuthal profiles in § 4.1). The presence of two distinct knots in this vicinity is known from

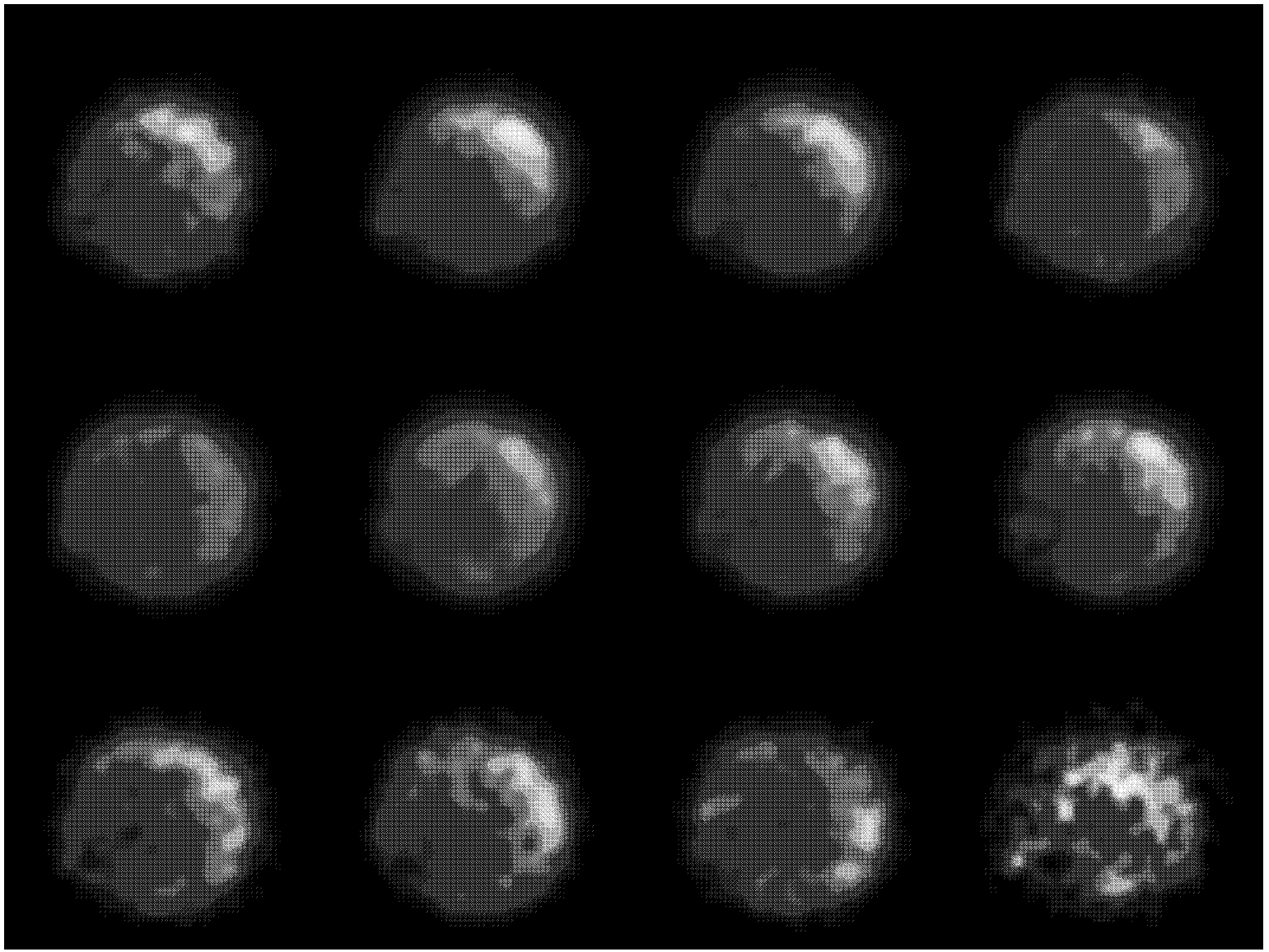

FIG. 4*a*

FIG. 4.—Narrowband images of Tycho obtained by *ASCA*. (*a*) Smoothed and exposure-corrected SIS images; (*b*) SIS images after deconvolution; (*c*) flat-fielded GIS images, with lower intrinsic spatial resolution, displayed on the same scale as the SIS images; (*d–f*) color versions of (*a–c*). From left to right, top to bottom, the images correspond to the following: *Top row*: low-energy lines ($E < 0.77$ keV); Fe L I; Fe L II; Mg Heα plus Fe. *Middle row*: continuum (1.4–1.7 keV); Si Heα; Si He $3p$; S Heα. *Bottom row*: S He $3p$ plus Ar; Ca Heα; continuum (4–6 keV); Fe Kα. See Table 1 for the energy cuts corresponding to each image.

FIG. 4*b*

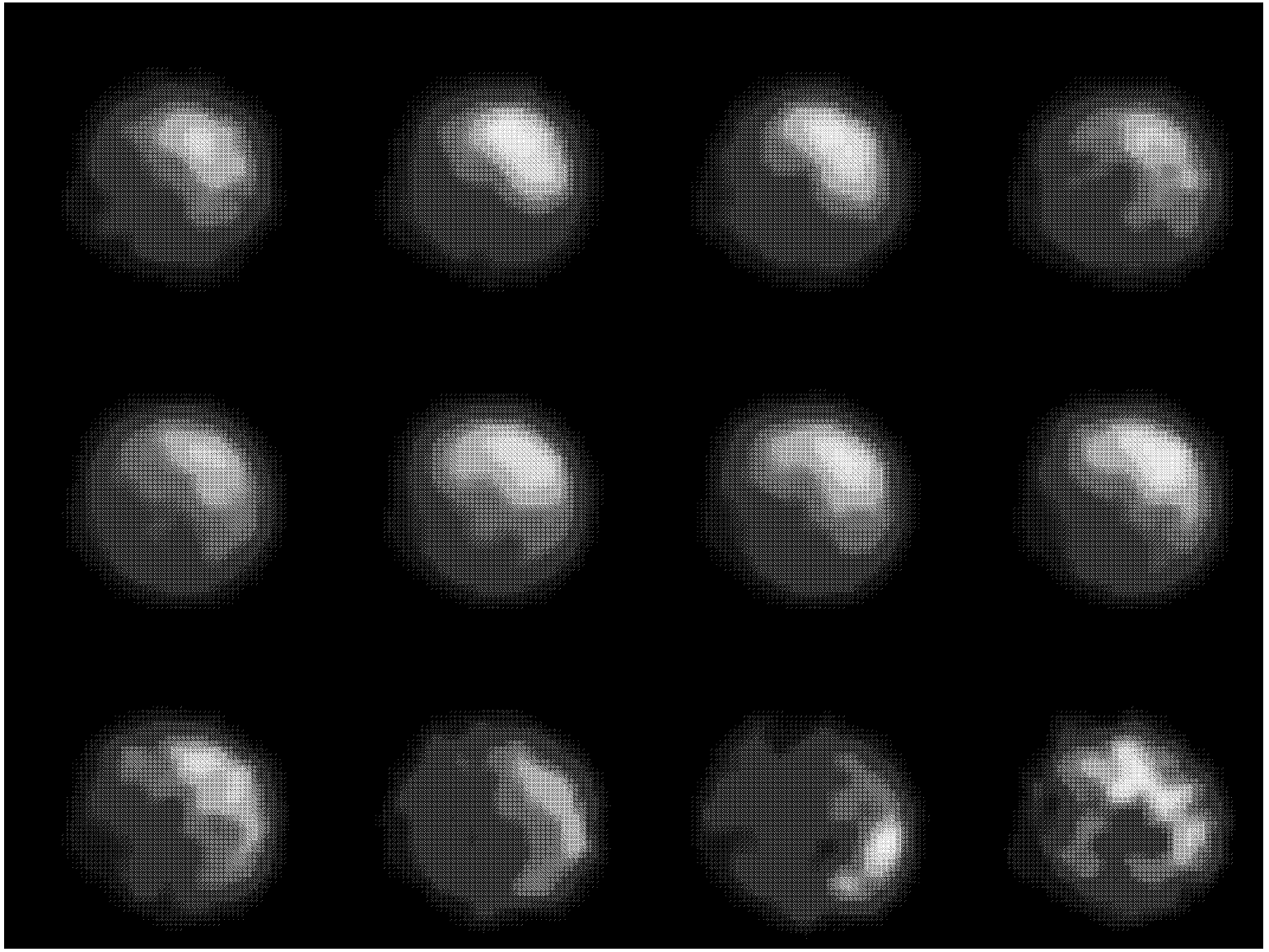

FIG. 4*c*

TABLE 2

LINE MODEL FOR SPECTRAL FITS

Line	Ion and Transition	Expected Energy (keV)	Fitted Energy (SIS0, C01) (keV)	Fitted Flux[a] (10^{-3} photons cm^{-2} s^{-1})
Si Heα.....	He, $n = 2 \rightarrow n = 1$	~1.86	1.859 (1.858–1.860)	52.7 (52.1–53.3)
Si He $3p$	He, $1s3p \rightarrow 1s^2$	2.182	2.185 (2.181–2.191)	4.38 (4.25–4.50)
Si He $4p$	He, $1s4p \rightarrow 1s^2$	2.294	...	0.55 × Si He $3p$
Si Lyα	H, $2p \rightarrow 1s$	2.006	...	1.49 (1.31–1.64)
Si Lyβ	H, $3p \rightarrow 1s$	2.377	...	0.14 × Si Lyα
S Heα	He, $n = 2 \rightarrow n = 1$	~2.45	2.448 (2.445–2.450)	13.6 (13.4–13.9)
S He $3p$	He, $1s3p \rightarrow 1s^2$	2.884	...	0.89 (0.81–0.96)
S He $4p$	He, $1s4p \rightarrow 1s^2$	3.033	...	0.56 × S He $3p$
S Lyα.....	H, $2p \rightarrow 1s$	2.623	...	0 (<0.13)
Ar Heα.....	He, $n = 2 \rightarrow n = 1$	~3.1	3.135 (3.120–3.147)	1.07 (0.99–1.15)
Ar He $3p$.....	He, $1s3p \rightarrow 1s^2$	3.685	...	0 (<0.060)
Ar He $4p$.....	He, $1s4p \rightarrow 1s^2$	3.875	...	0.57 × Ar He $3p$
Ca Heα.....	He, $n = 2 \rightarrow n = 1$	~3.85	3.818 (3.793–3.846)	0.53 (0.42–0.60)
Fe Kα	Several ions, $n = 2 \rightarrow n = 1$	~6.45	6.458 (6.432–6.485)	0.44 (0.39–0.50)

[a] $N_H \equiv 4.5 \times 10^{21}$ cm^{-2}, $kT_1 = 0.99$ keV [EM $\equiv 1/(4\pi d^2)\int n_e n_i\, dV = 6.0 \times 10^{13}$ cm^{-5}], $kT_2 \equiv 10$ keV (EM $= 4.1 \times 10^{12}$ cm^{-5}), $\chi^2 = 617.6$, dof $= 532$. Errors are the formal 90% confidence limits ($\Delta\chi^2 = 6.63$). The calibration of the energy scale is estimated to be accurate to about 0.5%–2%.

high spatial resolution broadband images. In their comparative study of the *Einstein* and *ROSAT* high-resolution images, Vancura et al. (1995) showed that the southern knot is more prominent in their Si–Fe band than in their Si–S band, while the northern knot is visible in both bands. All these data are consistent with the interpretation that the southern knot is dominantly Fe, while the northern knot is dominantly Si and S.

3. SPATIALLY INTEGRATED SPECTRUM

A study of the spatial variation of spectral parameters using narrowband images requires information that is not readily extracted from the images themselves. First, the images give only the total number of counts in a particular pulse-height range, where the total is the sum from the continuum, the line features of interest, and the nearby line features. Second, for Tycho, the available images give no practical information on the ionization state of the X-ray gas. The standard diagnostic for the ionization age is the relative strength of the Lyα and Heα lines, but the Lyα lines are not sufficiently resolved in the spectrum that we can isolate them from nearby spectral features in order to form images. These problems can be addressed by modeling the spatially integrated spectrum from the entire remnant obtained by the SIS instruments in order to obtain the average line intensities. We will thereby obtain benchmarks for all the interesting physical quantities, which can be compared later with their spatially localized values when we use the line images to search for nonuniformities in the spectrum. An alternative to our approach is to fit spectra region by region in order to characterize the spatial variations, but this approach is independent of narrowband images.

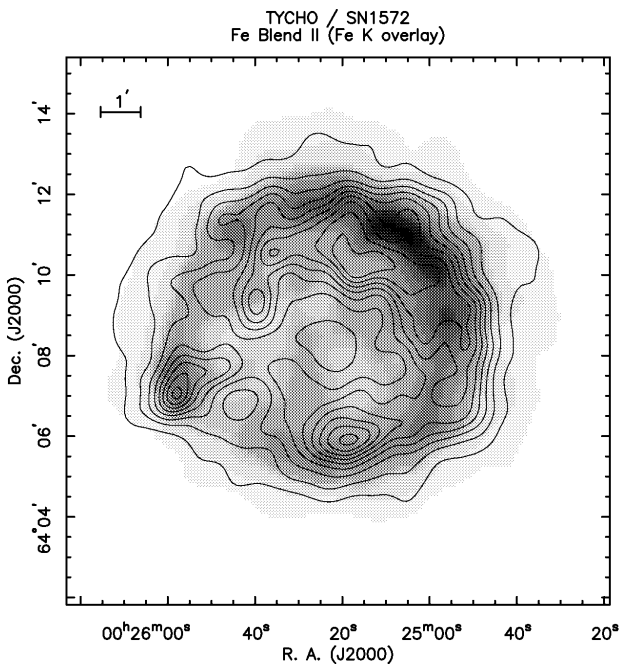

FIG. 5a

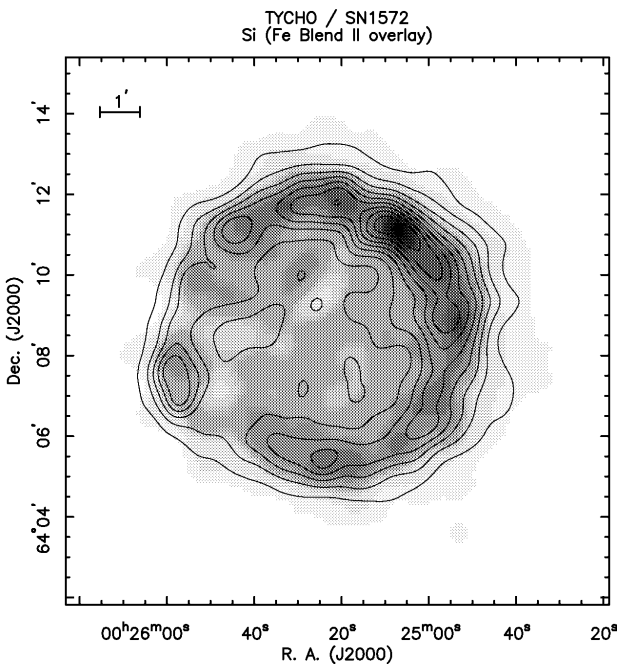

FIG. 5b

FIG. 5.—(*a*) Overlay of the intensity contours of Fe K onto the image of Fe L II. (*b*) Overlay of the intensity contours of Fe L II onto the image of Si Heα. The contours show linear 10% intensity increments.

For the spectral analysis, we use only the 2-CCD mode data. Although the 4-CCD mode data had a longer integration time, the 2-CCD mode data are less sensitive to errors and uncertainties in the calibration (Rasmussen et al. 1994; Dotani et al. 1995). The exposure times range from 3.7 to 7.2 ks after time-filtering. In 2-CCD mode, only two of the four chips comprising each SIS detector are exposed at a time, so that two separate exposures are required to cover the entire Tycho remnant. To allow the combination of spectra from individual chips, the gains were adjusted using the updated calibration file of 1996 February 29. We also use response matrices customized for each pulse-height spectrum (SISRMG; Crew et al. 1996). All the data within a 5′ radius from both exposures with the two SIS instruments are fitted jointly.

3.1. *Line Model*

The X-ray spectrum characteristic of supernova remnants is an optically thin thermal continuum, plus emission lines of highly stripped ions of the abundant elements. There may also be a nonthermal X-ray continuum component in Tycho that is due to synchrotron acceleration at the shock front (Ammosov et al. 1994; Koyama et al. 1995). Using *ASCA* spectra for energies above about 1.5 keV, it is possible to constrain the shape of the underlying continuum (if the plasma temperature is high enough) and reliably measure line strengths, since most prominent lines in this energy range are reasonably well-separated by the *ASCA* resolution. At lower energies, the confusion from the complex Fe L emission, which is not well-resolved by *ASCA*, plus greater complexity in the continuum shape, make it more difficult to measure line strengths reliably. In order to extract the line strengths in the most straightforward manner, we therefore fitted the observed spectrum above 1.5 keV, with the continuum modeled as two thermal bremsstrahlung components and all the important emission lines and line blends modeled as Gaussian features. We have included some weak emission lines in our model at fixed intensities relative to stronger lines in order to obtain the best consistency in our fit results. The energy scale is allowed to be separate for the pulse-height spectrum from each pair of CCDs in order to account for residual gain differences between the CCD chips after the calibration correction. The relative fluxes, line widths, and continuum parameters are required to be the same for all data sets.

Tycho's X-ray continuum clearly requires two components to account for the flux at high energies. Fink et al. (1994) show that the *Ginga* data strongly require a hard spectral component, although they do not constrain its parameters. We chose to model the continuum as two bremsstrahlung components, with the temperature of the harder component fixed at 10 keV because the Fe K/Fe L flux ratio suggests a high temperature (see § 3.3). We also considered a power law with spectral photon index 3.0 since this is the spectral index of the nonthermal component detected in SN 1006 (Koyama et al. 1995). For Tycho's spectrum above 1.5 keV, the line ratios used in our analysis vary by no more than several percent when these models for the hard continuum component are interchanged, or when the temperature of the hard thermal component is between 5.0 and 10.0 keV.

The lines and line blends included in our spectral models are listed in the first three columns of Table 2. In addition to the prominent Heα emission blends, we include the Lyα lines of Si and S, and the He $3p$ and $4p$ transitions of Ar. The Si feature at 2.2 keV is actually a blend of two He-like lines (He $3p$ at 2.182 keV and He $4p$ at 2.294 keV; see Table 2). The corresponding transitions in S occur at 2.884 and 3.033 keV, and the higher energy line is blended with Ar Heα. We model all the $3p$ and $4p$ transitions as separate features, but it is not feasible to fit the strengths of both lines independently because of their proximity to each other and to other stronger lines. Since the relative strengths of these two lines do not vary with ionization age, and vary by only 10%–20% over a decade in temperature, we fixed the intensity of the $4p$ line relative to that of the $3p$ line at its value at temperature 10^7 K (see Table 2). The average temperatures of Si and S are found to be near 10^7 K independent of this assumption.

We model the lines that contribute to the Heα blend as a single Gaussian feature. The resulting errors are small for a spectrum of comparable quality to the SIS spectrum of Tycho: less than about 10% for the total flux, and about 15 eV for the width of the Si blend. The error in the width is somewhat larger for Ar and Ca, whose constituent lines are farther apart in energy. The line centroids for the Heα blends were allowed to be fitted, while the energy scale of all the weaker lines was linked to that of the Si He $3p$ and $4p$ transitions. Line widths were forced to be equal for all lines of the same element and are generally on the order of 30–40 eV. Even for the highest estimates of the shock velocity in Tycho (Hamilton et al. 1986; J. P. Hughes 1996, private communication), the Doppler broadening should be only 15–20 eV for the Si and S lines. The larger observed width is due partly to a worse spectral resolution than is accounted for by the current response files (Rasmussen et al. 1994; Dotani et al. 1995).

The neutral hydrogen column density was fixed at 4.5×10^{21} cm^{-2}, the most recently measured value in the radio (Albinson et al. 1986). Use of a column density between 2.5×10^{21} cm^{-2} (the low end of radio estimates; Hughes, Thompson, & Colvin 1971) and 6.8×10^{21} cm^{-2} (the value fitted to the BBXRT spectrum by Vancura et al. 1995) affects the ratios of fitted Si, S, and Ca line intensities by no more than several percent.

The fitted line fluxes are shown in the final column of Table 2, with the 90% confidence ranges ($\Delta\chi^2 = 2.71$). The line energies fitted for SIS0, chips 0 and 1, are also shown in Table 2 with their formal errors. The calibration of the SIS energy scale, however, is estimated to be accurate only to 0.5%–2% (Dotani et al. 1995).

3.2. *Line Diagnostics*

Given a set of measured line intensities, interesting physical quantities are constrained by comparing appropriate line intensity ratios with theoretical calculations over a grid of parameter values. The most widespread use of this technique with X-ray data was with the *Einstein* focal-plane crystal spectrometer (FPCS), which observed narrow slices of the spectrum at high spectral resolution (for more details and examples, see, e.g., Canizares & Winkler 1981; Winkler et al. 1981; Flanagan 1990). As an example, the temperature may be constrained by comparing lines close in energy arising in the same ion of the same element, so that the dependence on other parameters, such as column density or ionization age, is minimized. For lines of different elements, a solar abundance of elements is assumed for the calculations. If the temperature and ionization age are already

well-constrained, the ratios of lines from different elements then constrain the relative element abundances relative to the solar value.

We calculate relative intensities for each pair of transitions under consideration for a grid of temperatures and ionization ages using the plasma emission code of Raymond & Smith (1977; 1992 version) coupled to the ionization code of Hughes & Helfand (1985). Since less ionized ions can contribute to the flux in the Heα blend via their $n = 2$ to $n = 1$ transitions, particularly in ionizing plasmas such as supernova remnants, we include emission from these lines using the atomic data parameters of Mewe, Gronenschild, & van den Oord (1985) following Hughes & Helfand (1985). We also include the contribution from satellites to the resonance line.

We consider the lines of Si, S, Ar, and Ca in this section. For Si and S, the temperature diagnostic is the ratio of He $3p(+4p)$ relative to Heα. Only the He $3p$ line is used for S since the He $4p$ line is blended with Ar. The ionization age diagnostic is the ratio of Lyα (H-like ion) relative to Heα (He-like ion). With constraints on these two parameters, the ratios of the Heα strengths of Si, S, Ar, and Ca are used to constrain the relative abundances of these elements, making the assumptions that the temperatures and ionization ages of Ar and Ca are consistent with those of Si and S, and that the neutral hydrogen column density is 4.5×10^{21} cm^{-2}. The measured 90% confidence limits on the spatially averaged diagnostic line ratios for Tycho are given in Table 3.

The regions of temperature–ionization age parameter space, where the calculated theoretical line strength ratios are consistent with the 90% confidence limits for the measured intensity ratios of He $3p(+4p)$/Heα and Lyα/Heα in Si (*solid lines*) and S (*dashed lines*), are shown in Figure 6. The He $3p(+4p)$/Heα ratio is seen to be a temperature diagnostic since its value is nearly independent of ionization age for a given temperature whenever the He-like ion is abundant (at ionization ages log nt [cm^{-3} s] > 10). The Lyα/Heα ratio, being a ratio between lines of two different ions, loses its dependence on the ionization age only when the ionization age approaches the equilibrium value for a given temperature. From the figure, we see that, for Si, the ionization age is $10.9 <$ log nt (cm^{-3} s) < 11.1 and the temperature is $6.92 <$ log T (K) < 6.97 (or $kT = 0.7$–0.8 keV); for S, the ionization age is log nt (cm^{-3} s) < 11.3, and the temperature is $6.95 <$ log T (K) < 7.06 (or $kT = 0.8$–1.0 keV). The values for S are therefore consistent with those for Si.

Strong constraints on the temperature and ionization age cannot be obtained for Ar and Ca since their He $3p$ and Lyα features are extremely weak in the Tycho spectrum. If He $3p$ lines are fitted for Ar and Ca, the 90% confidence limits for He $3p$/Heα give temperatures consistent with the Si and S temperatures. Likewise, the Lyα/Heα ratios for Ar and Ca give limits for the ionization age that are consistent with the ionization ages of both Si and S. We therefore assume that the temperatures of Si through Ca are all consistent, and that the ionization ages of Ar and Ca are consistent with both those of Si and S.

TABLE 3

SPATIALLY AVERAGED DIAGNOSTIC LINE RATIOS

Ratio	Fitted Value and 90% Limits
Si He ($3p + 4p$)/Si Heα.....	0.129 (0.124–0.134)
Si Lyα/Si Heα	0.028 (0.025–0.031)
S He $3p$/S Heα	0.065 (0.058–0.072)
S Lyα/S Heα	0 (<0.010)
S Heα/Si Heα	0.26 (0.25–0.27)
Ar Heα/Si Heα	0.020 (0.019–0.022)
Ca Heα/Si Heα	0.010 (0.008–0.012)

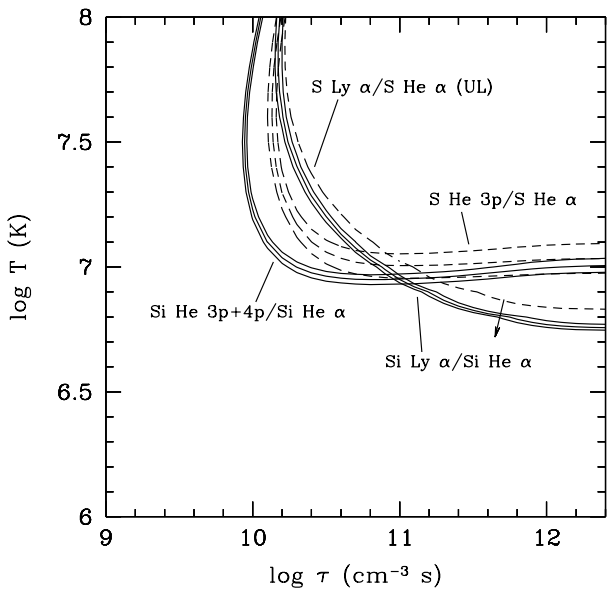

FIG. 6.—The region of temperature–ionization age (T-nt) parameter space allowed by the average measured line ratios in the SIS spectrum. The solid lines trace the values of log T and log nt that correspond to the best value and 90% confidence limits for the Si line intensity ratios He ($3p + 4p$)/Heα and Lyα/Heα; the dashed lines correspond to the limits for S. The single S Lyα/Heα contour corresponds to an upper limit. The region of overlap for all the contours is near log $nt = 10.9$ and log $T = 6.95$.

Having limited the possible range of temperature and ionization age, relative abundances of the elements may be estimated from the relative Heα line strengths. The abundance of S relative to Si is 1.1–1.6 times the solar value. The abundance of Ar relative to Si is roughly 0.4–1.3 times that of the solar value, assuming Ar has the same ionization age as Si. The abundance of Ca relative to Si is from 5 to more than 30 times the solar value, assuming that Ca has the same ionization age and temperature as Si. There is no strong enhancement of Ca relative to Si predicted for the nucleosynthesis yield of either Type I or Type II supernovae. A higher ionization age for Ca could reduce the required abundance enhancement, but this would then imply a much higher energy centroid for the blend than would be consistent with the observed centroid. It is more likely that much of the Ca is coming from hotter gas associated with the blast wave since the emissivity of the Ca line at higher temperatures is much increased over its value at temperatures ~ 1 keV, while the centroid is comparable to that observed. A similar conclusion will be reached regarding the Fe emission in the next section.

Although there is a feature near 1.3 keV that could be due to Mg, it may be blended with Fe emission. Since we did not model the spectrum below 1.5 keV, the question of the Mg abundance is deferred for more sophisticated spectral analysis.

In summary, we obtain the following results from the line diagnostics for the spatially averaged *ASCA* spectrum: (1) The temperatures are approximately equal for Si and S and in the range log T (K) = 6.92–7.06, and such temperatures

are consistent with the available data for Ar and Ca. (2) The ionization age of Si is approximately log nt (cm^{-3} s) = 10.9–11.1, and the ionization age of S is consistent with this. The ionization ages of Ar and Ca are consistent with those of Si and S, but their uncertainties are large. (3) Assuming that the temperatures and ionization ages of Si and S hold for the elements Si, S, Ar, and Ca, the abundance of S relative to Si is found to be roughly solar, while that of Ar relative to Si and S is consistent with the solar value with a large uncertainty. Formally, Ca has a high abundance relative to Si, but it is more likely that much of the Ca arises from hotter gas associated probably with the blast wave.

3.3. Fe *Emission*

We consider the emission from Fe separately in this section because there are indications that it arises under different physical conditions than that of other elements. Namely, the measured centroid of the Fe K blend is at a lower energy than predicted for the ionization age deduced for Si and S, while its intensity is too high to be consistent with the temperature deduced for Si and S for reasonable abundances. In addition to the Fe K emission, there is Fe L emission at energies of $\sim$1 keV. We did not attempt to fit for Fe L line intensities because of the limited spectral resolution of the SIS at the relevant energies, so we base our constraints on the ratio of counts in the energy bands corresponding to the narrowband images (see Table 1). Note that there are two nonoverlapping energy bands for Fe L. The theoretical Fe emission-line spectra are calculated in these energy bands, and folded with the energy-dependent effective area of the SIS and the interstellar absorption, in order to give predicted count rates for a range of temperatures and ionization ages. We also account for a detector resolution of about 50 eV FWHM. The theoretical count ratios are compared with the measured Fe K/Fe L count rate ratios after correction for the fraction of the counts in each energy band due to the continuum. For Fe L, this correction is estimated by extrapolating the continuum component in the fitted spectral model to energies below 1.5 keV. Since the Fe L and Fe K emission are so widely separated in energy, we considered a range of column densities from the current, best radio and X-ray measurements. For columns between 4.5×10^{21} cm^{-2} and 6.8×10^{21} cm^{-2}, the fraction of line to total counts in the Fe L bands varies by 15%–25%.

Allowing for a 20% uncertainty resulting from the continuum correction, the Fe K/Fe L I and Fe K/Fe L II average count ratios imply log T (K) = 7.6–8.3 and log nt (cm^{-3} s) = 9.9–10.6. Consistency with the 90% confidence limits for the energy centroid of the Fe K blend requires log $T \sim 7.8$ and log $nt \sim 10.1$. These parameters are clearly inconsistent with the parameters deduced for Si and S (log T = 6.92–7.06, log nt = 10.9–11.1), and imply that the Fe K emission in Tycho arises under conditions different from the intermediate-mass elements. These results support earlier spectral results (Hughes 1991; Petre et al. 1992; Vancura et al. 1995).

We have assumed that all the counts in the Fe L I and Fe L II bands are due to Fe. Observations with the *Einstein* FPCS (Hwang 1994) detect Ne Heα from the entire remnant and place an upper limit on Ne Lyα in the southern section of the remnant. If the fluxes within the rectangular FPCS apertures are scaled for the entire remnant using the *Einstein* HRI image, the *ASCA* count rates in Ne Heα make up only about 10% of the observed Fe L I count rate, whereas the upper limit for the flux of Ne Lyα corresponds to about 10% of the Fe L II count rate. We also assume that the Fe L and Fe K emission arise largely under the same physical conditions. This is true to some extent because Fe K emission is accompanied by significant Fe L emission at the relevant temperatures, but the narrowband images show that the Fe K emission is generally interior to the Fe L emission.

4. IMAGING RESULTS

4.1. *Spectral Variations from Azimuthal Brightness Profile Ratios*

Because the most prominent differences between the narrowband images occur with azimuthal angle, we show in Figure 7 azimuthal profiles of the deconvolved images for an annulus with inner and outer radii of 2′ and 5′ centered on the remnant. The number of counts in angular bins of 5° is plotted with purely statistical errors based on the number of counts in each bin. Angles are measured in degrees from the west (to the right in Fig. 4) with positive angles increasing counterclockwise. In § 3, we used the ratios of line strengths in the spatially integrated spectrum as diagnostics for the average temperature, ionization age, and relative element abundances. Here we use ratios of the azimuthal count profiles to search for spatial variations in these line ratios and in the corresponding physical parameters.

We scale the total image count ratios for the line features in He-like Si and S to the appropriate fitted global intensity ratios from § 3, and in Figure 8, we show the variation of these ratios with azimuthal angle. The error bars show statistical 1 σ errors, and the solid line shows the average ratio. For these (and other) ratios, a χ^2 test gives statistical inconsistency between the observed azimuth ratio profiles and a flat profile implying no spatial variation.

We assume that the intensity ratio of Lyα/Heα is constant with position throughout the remnant at the value measured in the spatially averaged spectrum so that the ionization age is constrained at each temperature as in Figure 6. We then infer that the temperature kT implied by the Si He $3p + 4p$/Si Heα ratio varies between 0.65 and 0.9 keV in the deconvolved image profiles. The undeconvolved profiles give a comparable, but slightly more modest, temperature variation between kT = 0.7–0.9 keV. The S He $3p$/S Heα image ratio implies temperatures kT between 0.7 and 1.2 keV, with an excursion up to 1.9 keV. In the undeconvolved profiles, the variation in temperature is between 0.8 and 1.2 keV.

We examine briefly how our assumptions affect the conclusions. We have assumed that the continuum fraction in a particular energy band is constant throughout the remnant. The relative strength of Si Heα to the adjacent low-energy continuum and of Ca Heα to the adjacent high-energy continuum show variations of less than a factor of 2, which result in errors of 10%–25% in the diagnostic ratios from assuming that the continuum fraction does not vary. We have assumed a constant column density, but variations in the column density are an unlikely explanation for the variations in the Si and S temperature diagnostics. The lines are sufficiently close in energy that no plausible variation in the column density can effect the observed variations. However, a variation in the column density may explain the factor of 2–3 observed variation in the spatial intensity of

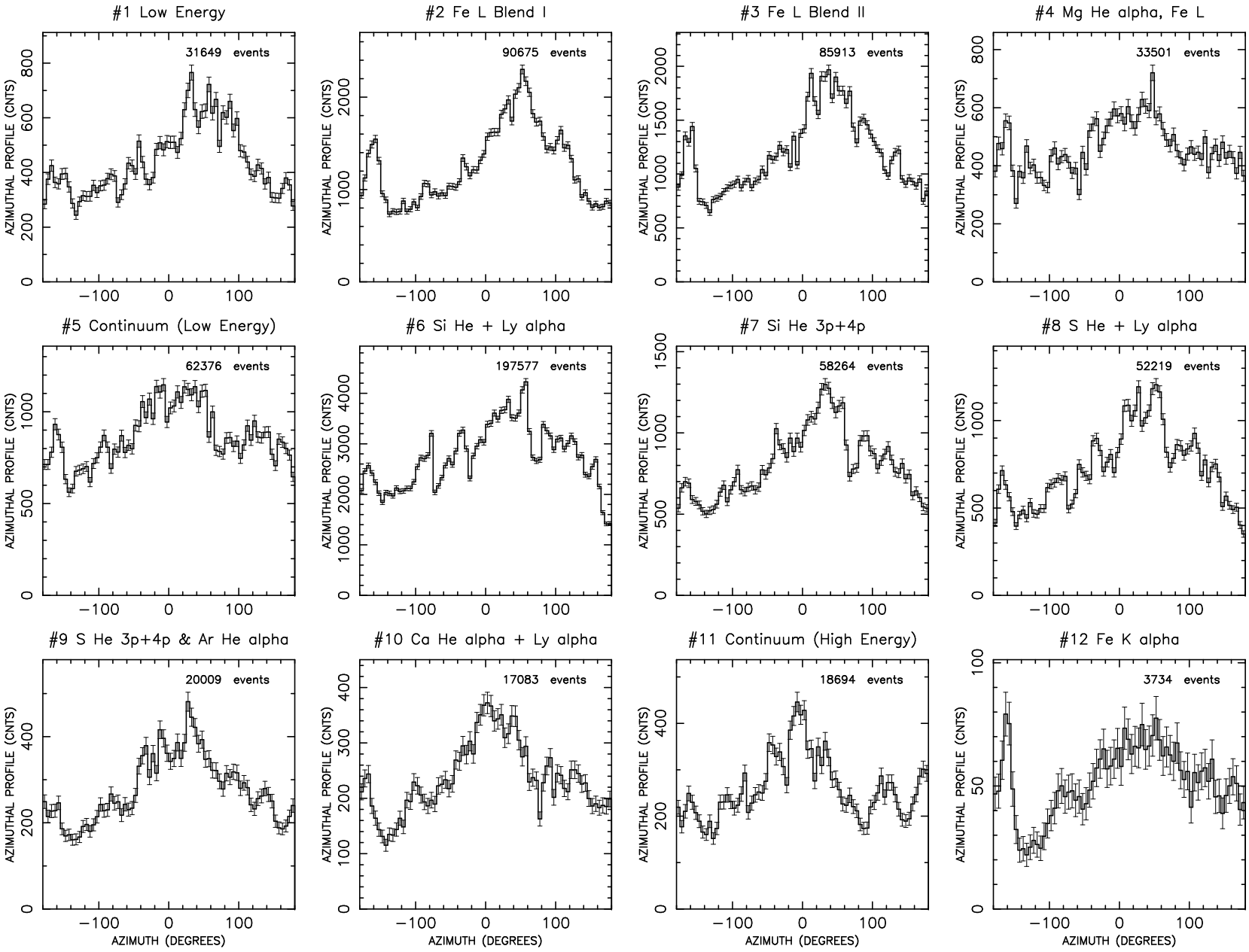

FIG. 7.—Azimuthal profiles of the deconvolved narrowband images in Fig. 4*b* for radii between 2′ and 5′ in angular bins of 5°

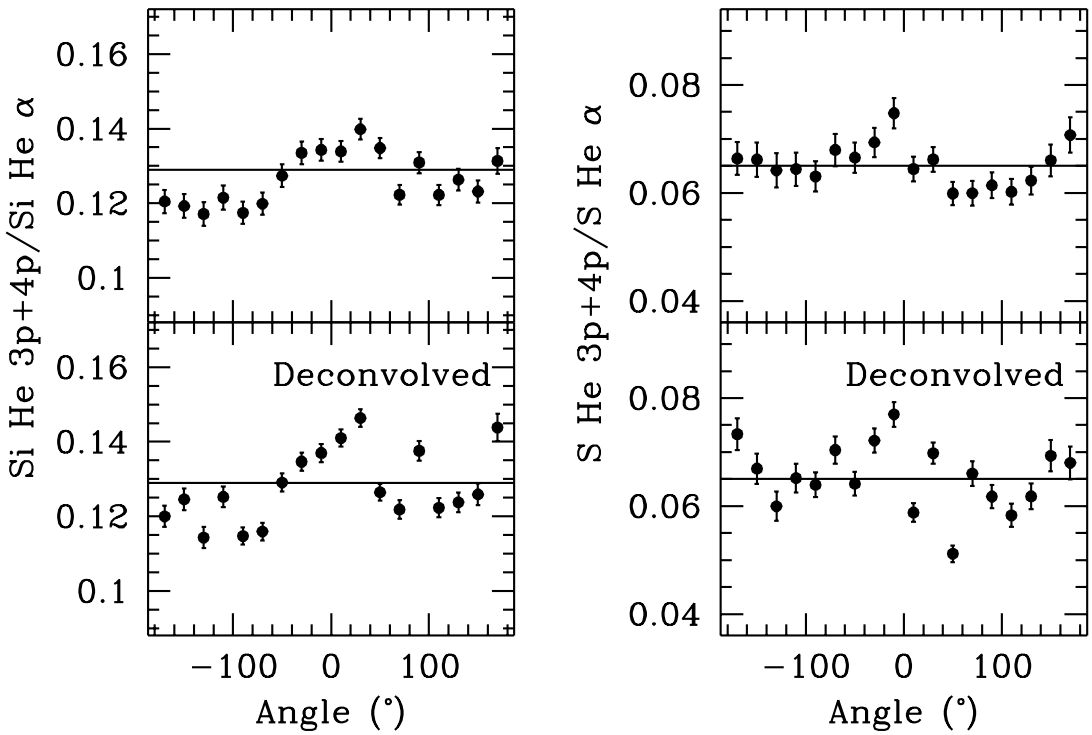

FIG. 8.—Ratios of azimuthal Si and S line profiles from Figs. 4*a* and 4*b* before and after deconvolution in angular bins of 20°

Fe K/Fe L. We assume that the ionization age is constant throughout the remnant because the Lyα lines are so weak that they cannot be resolved from the nearby Heα lines. Our conclusions on the temperature and abundance variation with position are therefore made with reservations, until future higher spatial and spectral resolution observations allow stronger constraints on the spatial variation in the ionization age.

4.2. *Geometric Models for Radial Profiles*

The radial profiles of the deconvolved images are generally similar to each other, except that the Fe K profile clearly peaks at a smaller radius than the others (see Fig. 9). To further study the three-dimensional geometry of the emitting region, we fitted the undeconvolved, exposure-corrected radial profiles of each narrowband image to that of a uniformly emitting spherical shell. The shell is projected onto the plane of the sky, a constant sky background added, the resultant image convolved with the PSF of the X-ray mirrors, and the total counts normalized to the data. Radial profiles for the model image are then calculated in 0.25 bins and compared with the measured profiles, with statistical errors based on the number of counts in each bin. A two-dimensional parameter grid for the inner and outer radii was searched. Most of the fits are statistically unacceptable, with χ_r^2 greater than several, and the poorness of the fit is most likely due to the need for a more sophisticated model since azimuthal variations are known to exist.

Nevertheless, the results of our fits allow a simple characterization of the radial extent of the emitting region for each spectral feature, and these are all found to overlap. The outer radius is nearly constant at about 4.5 in all the fits, while there is a significant difference in the fitted inner radius for several of the images ranging from about 2.1 (for Fe K) to 3.2. The inner radii for Fe L, Si, and S, which range from 2.6 to 3.2, are in reasonable agreement with the inner radius 2.88 of the ejecta shell in the double shell model of Seward et al. (1983) for the *Einstein* HRI data. Our large outer radius (4.5) is an artifact since the remnant is known to extend only to a radius of 4′.

Using the same procedures as for the spherical shell model, fits to a face-on ring are found to give significantly worse fits for the Si Heα image, suggesting that the X-ray–emitting geometry for Tycho is more consistent with a spherical shell than with a face-on ring. Any inclination of such a ring is not likely to be large given Tycho's circular morphology.

5. SEARCH FOR SYSTEMATIC DOPPLER SHIFTS

We searched for systematic shifts in line energy across the face of the remnant by fitting the centroids of the Si and S Heα blends in overlapping 1′ × 1′ boxes. We use the 4-CCD mode data for maximum signal-to-noise. There are gain differences among the four chips of each SIS sensor that are not fully corrected by the current calibration, so we scaled the energies for each chip relative to a reference chip in order to give a smooth distribution of energies across the chip boundaries. There are no statistically significant shifts in the line centroids. For a shock velocity of about 2000 km s^{-1} estimated from the optical data by Smith et al. (1991), the magnitude of the expected line energy shift is about 12 eV for the Si line. This is significantly larger than the typical error on our centroid measurements. The optically determined shock velocity, which is based on spectral observations of a single knot, may underestimate the average shock velocity since there is significant variation with position of the H Balmer line widths that determine the shock velocity. Radio measurements give a current expansion velocity of 3600 km s^{-1} (Strom et al. 1982; Tan & Gull 1985), for a distance of 3 kpc, which requires even larger

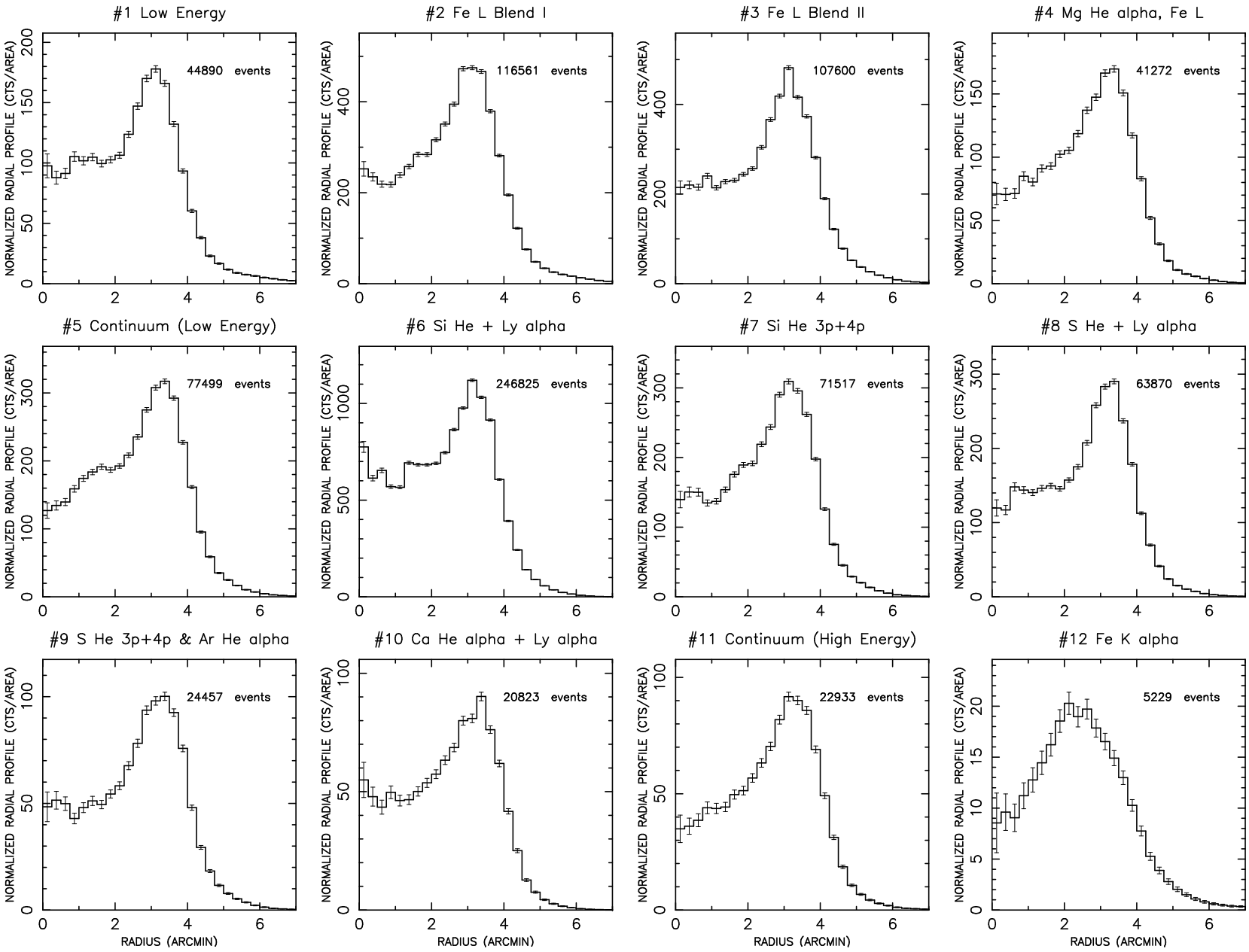

FIG. 9.—Radial profile of the deconvolved narrowband images from Fig. 4*b* for radial bins of 0.25

energy shifts. Hamilton et al. (1986) also deduce a higher shock velocity of about 5000 km s^{-1} from their modeling of the X-ray spectrum. Relative to Cas A, where systematic Doppler shifts are observed between two halves of the remnant and imply a ringlike geometry (Markert et al. 1983; Holt et al. 1994), the absence of such shifts in Tycho suggests that its geometry is either spherically symmetric or, if a ring, oriented face-on. The radial-fitting results, however, favor a spherical geometry.

6. DISCUSSION

In this section, we will address issues regarding the ionization age of Si and S, stratification and mixing of the ejecta, and the origin of the Fe emission.

The global ionization ages we obtain for Si and S (log nt [cm^{-3} s] $\sim$ 11) are higher than those obtained by Hughes (1991) with the *Einstein* solid-state spectrometer (SSS) and *Tenma* and by Vancura et al. (1995) with the BBXRT (log $nt \sim 10$). Hughes (1991) based his results on the measured energy centroids of the Kα blends (including He- and H-like ions) for a temperature of $kT = 1.9$ keV deduced from fitting a thermal bremsstrahlung continuum. Vancura et al. (1995) fitted an NEI model to the data below 5 keV and obtained a temperature of 1.7 keV; in this fit, the ionization age is again determined primarily by the centroids of the Kα blends. Because the Si centroid changes only by a few eV over more than a decade in nt, the constraint on the ionization age from the centroid depends crucially on knowing the energy scale with high accuracy. The Lyα line that could set the energy scale unambiguously is so weak in Tycho that it is dwarfed by the nearby Heα lines. The temperature determined from the continuum shape alone is subject to error as well, since there is an additional hard component in the spectrum.

We feel that it is therefore more reliable to constrain the ionization age jointly with the temperature from line ratios. Our results are insensitive to the continuum model, since all spectral parameters are determined from ratios of Si and S lines that are clear of the thicket of Fe L lines that starts below 1.5 keV. When we carry out an analysis of line ratios in the BBXRT data, we find that the constraints on the average temperature and ionization age of Si and S are consistent with those obtained here with the SIS. A temperature as high as 1.7 keV would require roughly a 50% error in the measured SIS Si line ratio, whereas the maximum systematic error at 2.2 keV is probably $\lesssim$20%.

Immediately following the supernova event, the ejecta of Type I remnants are expected to be stratified in layers, with Fe and Ni in the innermost layer, a mixture of Si, S, and other intermediate-mass elements in the intermediate layer, and unburned material in the outermost layer (Nomoto, Thielemann, & Yokoi 1984). This structure, however, may be disrupted during the subsequent evolution of the remnant. The various images of Tycho in different Si and S line features are similar in their gross spatial characteristics, in accord with the expectation that these elements should be well-mixed. Their temperatures and ionization ages are consistent, also indicating that these elements are under similar physical conditions. In our spherical shell models for the radial profiles, the emitting regions all overlap in radius and therefore indicate that some mixing has occurred between the radial layers that emit in Si and S and in Fe. The Fe L images show a radial extent comparable to that of the Si and S images. The fitted radii for the Fe K image are also compatible with the others, but the image itself shows that it is relatively brighter in the interior regions. Unfortunately, a detailed comparison is hampered by the sparse counts in the Fe K image.

The overall strength of Fe K intensity relative to Fe L and the position of the Fe K energy centroid requires that the Fe-emitting plasma be hotter and less ionized than the rest of the remnant. This is in general agreement with previous spectral studies of Tycho, which show that the Fe emission arises under singularly different conditions than emission from other elements (Hughes 1991; Petre et al. 1992). Hughes (1991) suggests that the Fe ejecta is localized in the inner regions of the remnant, less recently shocked, and therefore at a lower ionization age. Hydrodynamic models have explained the high Fe K flux by mixing the Fe ejecta radially outward into higher temperature zones (Hamilton et al. 1986; Itoh et al. 1988; Brinkmann et al. 1989), but of these, the latter two (Itoh et al. 1988; Brinkmann et al. 1989) were compared only to data with a bandpass above 1 keV and thus lacked constraint by the Fe L emission.

The high temperature and relatively lower ionization age of Fe are consistent qualitatively with a density in the ISM lower than in the Si and S ejecta, in which case the higher temperature component would represent the blast shock that is distinguished from the ejecta-dominated reverse shock that dominates most of the X-ray emission. However, it is also possible that the Fe K emission arises in the ejecta, and that the low-ionization age indicates that the Fe ejecta is confined to the inner layers and has been shocked only recently. This then requires an explanation for why the Fe is so much hotter than the Si. The high temperature may favor the origin of Fe in the blast wave. Detailed modeling of the spectrum, including the Fe L region near 1 keV, is required to make definitive statements about the nature of the Fe emission. A final possibility is that the dust that is known to be present from the remnant's infrared emission (Saken, Fesen, & Shull 1992) is producing fluorescent Fe K emission (Borkowski & Szymkowiak 1996).

All the available X-ray data support the low-ionization age of Fe, but our data do not necessarily support the conclusion that the Fe emission arises from the ejecta itself. However, it seems likely that the Fe ejecta has retained some of its stratification. A lower ionization age for Fe is clearly indicated by the data. If the Fe arises in the ejecta, it has been shocked recently, and therefore it is interior to the other elements. If the Fe emission arises in the blast wave, then the Fe ejecta must not yet have been shocked to X-ray–emitting temperatures, again indicating that the Fe ejecta is confined to the inner layers.

Finally, it is interesting to make a quick comparison of Tycho with Cas A, another famous young remnant, but of Type II. First, Tycho shows no detectable Doppler shifts across itself and is consistent with a spherical geometry, while Cas A shows a pattern of line energy shifts that is well-modeled by a ring geometry (Markert et al. 1983; Holt et al. 1994). Second, Tycho shows a very different pattern of brightness enhancements in the 4–6 keV X-ray continuum and the radio, while in Cas A, these are in good agreement. This may have implications for the relative importance of nonthermal X-ray emission from the shock wave in these two remnants. It will be of great interest to study the ejecta structure of young remnants in a consistent way in order to make comparisons.

7. SUMMARY AND CONCLUSIONS

We use the combined capability for spectroscopy and imaging available with the SIS on *ASCA* to map the Tycho supernova remnant in its X-ray emission features. For the first time, we have a picture of how line emission is distributed spatially in the remnant. Previous X-ray–imaging spectrometers lacked the requisite combination of spectral and spatial resolution, while observations of Tycho at other wavelengths show very little line emission to trace the distribution of matter in the remnant. The synchrotron radio emission is insensitive to the species of atoms present, while the optical emission is almost exclusively in the Balmer lines of hydrogen.

Although previous spectral studies have been unable to detect any significant changes in the spectrum across the Tycho remnant, the *ASCA* images clearly show relative differences in the brightness of emission lines across the remnant that require differences in the temperatures of Si and S of roughly 50% around the rim of the remnant, assuming that the ionization age is constant throughout the remnant. It is in fact likely that the ionization age varies with position, but our data do not sufficiently constrain this variation.

Tycho's circular shape suggests that the emitting geometry is either a spherical shell or a torus, in the simplest approximation. Fits to the radial profiles support a spherical geometry, as do the absence of significant systematic Doppler shifts across the remnant and the results of the *Einstein* HRI image analysis (Seward et al. 1983). However, more sophisticated treatment of azimuthal asymmetries, individual clumps, and a complicated shock structure is clearly required.

Our results show that there are modest variations in the spectral parameters with position in the remnant. We do not find firm evidence for the stratification of elements, but we do find that the Fe is peaked interior to the other emission and is in a singular physical state with higher temperature and lower ionization age than the other elements. The Fe ejecta is probably still confined to the inner ejecta layers.

Many spectral issues remain to be addressed. A definitive answer on the nature of the Fe K emission line must at least be deferred to a fit of a nonequilibrium ionization model to the entire *ASCA* spectrum, including the Fe L region, which provides very important constraints on the Fe K emission. NEI modeling of the *ASCA* spectrum of other remnants has revealed a hitherto unknown complexity in the spectrum, requiring, for example, multiple ionization ages (Hayashi et al. 1994). The simple one-component NEI models used with success in the past may finally have reached their limitations with *ASCA* data. This issue is further complicated by the nature of the continuum above 5 keV. The need for a hard component in the X-ray spectrum has been noted for some time and is in fact responsible for the rather different spectral parameters inferred by instruments sensitive at low energies compared with those sensitive only at high energies (compare, e.g., Becker et al. 1980 using the *Einstein* SSS with Smith et al. 1988 using *EXOSAT*). We now know that the situation is even more complicated than the simple question of whether there is or is not a component due to the blast wave. There may be a nonthermal component in X-rays due to Fermi acceleration at the shock front, as was found for SN 1006 (Koyama et al. 1995) and as is predicted for Tycho (Ammosov et al. 1994). Hydrodynamical simulations may be necessary to make sense of the increasing complexity of the spectral parameter space.

Spectral imaging with *ASCA* offers a tantalizing view of what will ultimately be possible with narrowband X-ray imaging of supernova remnants. With the scheduled launch of the *Advanced X-Ray Astrophysics Facility*, 0.″5 imaging will be possible with comparable spectral resolution to the *ASCA* SIS, making the structure in Tycho's Fe K emission apparent without image restoration. Because remnants radiate the bulk of their thermal energy in X-rays, detailed information on the spatial variation of X-ray line emission provides critical information on the spatial variation of the spectral parameters through line diagnostics like those we have applied here. Ultimately, we can hope to unravel the two-dimensional abundance distribution of the ejecta and provide constraints for modelers of supernova explosions.

We are especially grateful to T. H. Markert for his perceptive comments on early manuscripts, and to J. P. Hughes for scientific discussions and the use of his ionization code. We also thank C. Canizares for his suggestions for testing the image deconvolution, R. Petre, K. Borkowski, and O. Vancura for scientific discussions, K. C. Gendreau, T. Yaqoob, and K. Mukai for discussion of *ASCA* calibration issues, and the referee, F. Seward, for many suggestions. John Dickel graciously provided his 22 cm radio data. U. H. thanks the NAS/NRC for support through a research associateship.

REFERENCES

Albinson, J. S., Tuffs, R. J., Swinbank, E., & Gull, S. F. 1986, MNRAS, 219, 427
Ammosov, A. E., Ksenofontov, L. T., Nikolaev, V. S., & Petukhov, S. I. 1994, Astron. Lett., 20, 157
Becker, R. H., Holt, S. S., Smith, B. W., White, N. E., Boldt, E. A., Mushotzky, R. F., & Serlemitsos, P. J. 1980, ApJ, 235, L5
Borkowski, K., & Szymkowiak, A. E. 1996, BAAS, 188, 7411
Brinkmann, W., Fink, H. H., Smith, A., & Haberl, F. 1989, A&A, 221, 385
Canizares, C. R., & Winkler, P. F. 1981, ApJ, 246, L33
Crew, G., et al. 1996, SISRMG, FTOOLS Software Package, HEASARC (Greenbelt: NASA/GSFC) (ftp: legacy.gsfc.nasa.gov)
Day, C. S., Arnaud, K. A., Ebisawa, K., Gotthelf, E. V., Ingham, J., Mukai, K., & White, N. 1995, ABC Guide to *ASCA* Data Reduction, *ASCA* Guest Observer Facility (Greenbelt: NASA/GSFC)
Dickel, J. R., & Jones, E. M. 1985, ApJ, 288, 707
Dickel, J. R., van Breugel, W. J. M., & Strom, R. G. 1991, AJ, 101, 2151
Dotani, T., Yamashita, A., Rasmussen, A., & SIS Team. 1995, *ASCA* News, 3, 25
Fink, H. H., Asaoka, I., Brinkmann, W., Kawai, N., & Koyama, K. 1994, A&A, 283, 635
Flanagan, K. A. 1990, Ph.D. thesis, MIT
Gorenstein, P., Harnden, R., & Tucker, W. 1974, ApJ, 192, 661
Gotthelf, E. V. 1993, CLEANSIS, FTOOLS Software Package, HEASARC (Greenbelt: NASA/GSFC) (ftp: legacy.gsfc.nasa.gov)
———. 1994, ASCAEXPO, FTOOLS Software Package, HEASARC (Greenbelt: NASA/GSFC) (ftp: legacy.gsfc.nasa.gov)
Gotthelf, E. V., & Hwang, U. 1996, MPE Rep. 263, 257
Gotthelf, E. V., Jalota, L., Mukai, K., & White, N. E. 1994, ApJ, 436, L91
Gronenschild, E. H. B. M., & Mewe, R. 1982, A&AS, 48, 305
Hamilton, A. J. S., Sarazin, C. L., & Szymkowiak, A. E. 1986, ApJ, 300, 713
Hayashi, I., Koyama, K., Ozaki, M., Miyata, E., Tsunemi, H., Hughes, J. P., & Petre, R. 1994, PASJ, 46, L121
Holt, S. S., Gotthelf, E. V., Tsunemi, H., & Negoro, H. 1994, PASJ, 46, L151
Hughes, J. P. 1991, Supernovae, ed. S. E. Woosley (New York: Springer), 661
Hughes, J. P., & Helfand, D. J. 1985, ApJ, 291, 544
Hughes, M. P., Thompson, A. R., & Colvin, R. S. 1971, ApJS, 23, 323
Hwang, U. 1994, Ph.D. thesis, MIT
Itoh, H., Masai, K., & Nomoto, K. 1988, ApJ, 334, 279
Jalota, L., Gotthelf, E. V., & Zoonematkermani, S. 1993, Proc. SPIE, 1945, 453

Kirshner, R. P., Winkler, P. F., & Chevalier, R. A. 1987, ApJ, 315, 135
Koyama, K., Petre, R., Gotthelf, E. V., Hwang, U., Matsuura, M., Ozaki, M., & Holt, S. S. 1995, Nature, 378, 255
Lucy, L. 1974, AJ, 79, 745
Markert, T. H., Canizares, C. R., Clark, G. W., & Winkler, P. F. 1983, ApJ, 268, 134
Mewe, R., Gronenschild, E. H. B. M., & van den Oord, G. H. J. 1985, A&AS, 62, 197
Nomoto, K., Thielemann, F.-K., & Yokoi, K. 1984, ApJ, 286, 644
Petre, R., et al. 1992, UV and X-ray Spectroscopy of Laboratory and Astrophysical Plasmas, ed. E. Silver & S. Kahn (Cambridge: Cambridge Univ. Press), 424
Rasmussen, A., Crew, G., Ricker, G., & SIS Team. 1994, *ASCA* News, 2, 18
Raymond, J. C., & Smith, B. W. 1977, ApJS, 35, 419
Reid, P. B., Becker, R. H., & Long, K. S. 1982, ApJ, 261, 485
Richardson, W. H. 1972, J. Opt. Soc. Am., 62, 55
Saken, J. M., Fesen, R. A., & Shull, J. M. 1992, ApJS, 81, 715
Seward, F. D., Gorenstein, P., & Tucker, W. 1983, ApJ, 266, 287
Smith, A., Davelaar, J., Peacock, A., Taylor, B. G., Morini, M. 1988, ApJ, 325, 288
Smith, R. C., Kirshner, R. P., Blair, W. P., & Winkler, P. F. 1991, ApJ, 375, 652
Strom, R. G., Goss, W. M., & Shaver, P. A. 1982, MNRAS, 200, 473
Szymkowiak, A. 1985, Ph.D. thesis, Univ. Maryland
Tan, S. M., & Gull, S. F. 1985, MNRAS, 216, 949
Tanaka, Y., Inoue, H., & Holt, S. S. 1994, PASJ, 46, L37
Teske, R. J. 1990, ApJ, 362, 563
Tsunemi, H., Yamashita, K., Masai, K., Hayakawa, S., & Koyama, K. 1986, ApJ, 306, 248
Vancura, O., Gorenstein, P., & Hughes, J. P. 1995, ApJ, 441, 680
Winkler, P. F., Canizares, C. R., Clark, G. W., Markert, T. H., & Petre, R. 1981, ApJ, 245, 574
Wood, C. A., Mufson, S. L., & Dickel, J. R. 1992, AJ, 103, 1338